AGN–starburst connection in NGC 7582: Gemini near-infrared spectrograph integral field unit observations

Rogemar A. Riffel,[1][★] Thaisa Storchi-Bergmann,[1] Oli L. Dors, Jr[1] and Cláudia Winge[2]

[1]*Universidade Federal do Rio Grande do Sul, IF, CP 15051, Porto Alegre 91501-970, RS, Brazil*
[2]*Gemini Observatory, c/o AURA Inc., Casilla 603, La Serena, Chile*

ABSTRACT

We analyse two-dimensional near-infrared K-band spectra from the inner $660 \times 315\,\mathrm{pc}^2$ of the Seyfert galaxy NGC 7582 obtained with the Gemini near-infrared spectrograph integral field unit at a spatial resolution of $\approx 50\,\mathrm{pc}$ and spectral resolving power $R \approx 5900$. The nucleus harbours an unresolved source well reproduced by a blackbody of temperature $T \approx 1050\,\mathrm{K}$, which we attribute to emission by circumnuclear dust located closer than $25\,\mathrm{pc}$ from the nucleus, with a total mass of $\approx 3 \times 10^{-3}\,\mathrm{M}_\odot$. Surrounding the nucleus, we observe a ring of active star formation, apparently in the Galactic plane, with a radius of $\approx 190\,\mathrm{pc}$, an age of $\approx 5\,\mathrm{Myr}$ and a total mass of ionized gas of $\approx 3 \times 10^6\,\mathrm{M}_\odot$. The radiation of the young stars in the ring accounts for at least 80 per cent of the ionization observed in the Brγ emitting gas, the remaining being due to the radiation emitted by the active nucleus. The stellar kinematics was derived using the CO absorption band at $2.29\,\mu\mathrm{m}$ and reveals: (i) a distorted rotation pattern in the radial velocity field with kinematic centre apparently displaced from the nuclear source by a few tens of parsec; (ii) a high-velocity dispersion in the bulge of $\sigma_* = 170\,\mathrm{km\,s^{-1}}$ and (iii) a partial ring of $\sigma_* = 50\,\mathrm{km\,s^{-1}}$, located close to the Brγ emitting ring, but displaced by $\approx 50\,\mathrm{pc}$ towards the nucleus, interpreted as due to stars formed from cold gas in a previous burst of star formation. The kinematics of the ionized gas shows a similar rotation pattern to that of the stars, plus a blueshifted component with velocities $\geq 100\,\mathrm{km\,s^{-1}}$ interpreted as due to an outflow along the ionization cone, which was partially covered by our observations. The mass outflow rate in the ionized gas was estimated as $\dot{M}_{\mathrm{H\,II}} \approx 0.05\,\mathrm{M}_\odot\,\mathrm{yr}^{-1}$, which is one order of magnitude larger than the accretion rate to the active galactic nuclei (AGN), indicating that the outflowing gas does not originate in the AGN, but is instead the circumnuclear gas from the host galaxy being pushed away by a nuclear outflow. The flux distribution and kinematics of the hot molecular gas, traced by the $H_2\,\lambda\,2.22\,\mu\mathrm{m}$ emission line, suggest most of this gas is in the Galactic plane. An excess blueshift along PA $\approx -70°$, where a nuclear bar has been observed, can be interpreted as an inflow towards the nucleus. We thus conclude that the H_2 kinematics traces the feeding of the AGN, while the ionized gas kinematics traces its feedback via the outflows. An AGN–starburst connection in the nucleus of NGC 7582 is supported by the ratio between the mass accretion rate and the star formation rate in the circumnuclear region of ≈ 0.26 per cent, which is close to the expected relation between the mass of the supermassive black holes and that of the host galaxy bulge in galaxies (the Magorrian relation).

Key words: galaxies: individual: NGC 7582 – galaxies: kinematics and dynamics – galaxies: Seyfert – galaxies: starburst – infrared: galaxies.

1 INTRODUCTION

Many recent studies on the stellar population in the vicinity of active galactic nuclei (AGN) report an excess of young to in-termediate age stars in the inner few hundred parsec when compared to non-active galaxies (e.g. Heckman et al. 1997; González Delgado et al. 1998; Schmitt & Kinney 2000; Cid Fernandes et al. 2001; Storchi-Bergmann et al. 2001; Kauffmann et al. 2003; Cid Fernandes et al. 2005; Davies et al. 2007). This excess supports the existence of the so-called AGN–starburst connection (Perry & Dyson 1985; Terlevich & Melnick 1985; Norman & Scoville 1988;

★E-mail: rogemar@ufrgs.br

Cid Fernandes & Terlevich 1995), which can be understood as due to the fact that both the circumnuclear star formation and the nuclear activity feed on gas inflowing towards the nuclei of galaxies. The gas inflow, if massive enough, in its way to the centre, may trigger the circumnuclear star formation and, reaching the nucleus, also the nuclear activity. Alternatively, there may be a delay in the triggering of the nuclear activity, which would be fed via mass loss from the evolving stars. The AGN–starburst connection is consistent and somewhat expected within the presently favoured scenario of co-evolution of galaxies and their nuclear supermassive black holes (SMBH), supported by the M–σ relation (Tremaine et al. 2002; Ferrarese & Merrit 2000; Gebhardt et al. 2000): if the bulge grows via the formation of new stars (starbursts), and the SMBH grows via mass accretion from its surroundings, one could expect a relation between the nuclear mass accretion rate and the star formation rate (SFR) in circumnuclear starbursts.

The mechanism through which the gas makes its way from the circumnuclear regions of star formation – which in many cases have a ring-like morphology – to the AGN is nevertheless still elusive. In Simões Lopes et al. (2007), using optical images obtained with the *Hubble Space Telescope* (*HST*) of the inner few hundred parsec of both active and non-active galaxies, the authors concluded that there is a strong correlation between the presence of dusty structures (spirals and filaments) and nuclear activity in early-type galaxies, proposing that these structures trace the material in its way in to feed the active nucleus. Recently, this was shown to be the case for at least two low-activity AGN with circumnuclear rings of star formation: NGC 1097 (Fathi et al. 2006) and NGC 6951 (Storchi-Bergmann et al. 2007). In these two galaxies, the authors have observed streaming motions along nuclear spirals in the Hα emitting gas. Another similar case is the Seyfert galaxy NGC 4051 where Riffel et al. (2008) found streaming motions along a nuclear spiral in molecular gas emitting the $H_2 \lambda 2.1218 \mu m$ line.

Inflows towards AGN are difficult to observe, particularly in ionized gas, due to the predominance of emission from the outflowing gas in the vicinity of the active nucleus. The inflow probably occurs mostly in 'cold' gas, while the outflows are seen in ionized gas (e.g. Crenshaw & Kraemer 2000; Das et al. 2005; Das et al. 2006; Riffel et al. 2006). Studies aimed to investigate the kinematics and flux distributions of the molecular and ionized gas in the near-infrared (near-IR) bands indeed reveal that the H_2 emitting gas usually has a distinct kinematics and distribution from that of the ionized gas. The H_2 kinematics seems to be 'colder' and, together with the flux distribution, suggests that the molecular gas is more restricted to the Galactic plane, while the ionized gas seems to extend to higher galactic latitudes and has a 'hotter' kinematics (Storchi-Bergmann et al. 1999; Rodríguez-Ardila et al. 2004; Rodríguez-Ardila, Riffel & Pastoriza 2005a; Riffel et al. 2006, 2008). These studies suggest that the feeding of AGN is dominated by inflow of cold molecular gas, while the ionized gas contributes mostly to its feedback via the outflows.

This work is aimed at investigating the relation between circumnuclear star formation and nuclear activity, as well as to look for the mechanisms of feeding and feedback in the nearby Seyfert galaxy NGC 7582, which has a Hubble type SBab and has a distance of 21.6 Mpc [for $z = 0.00525$ from de Vaucouleurs et al. (1991), with 1.0 arcsec corresponding to ≈105 pc at the galaxy, adopting $H_0 = 73 \, km \, s^{-1} \, Mpc^{-1}$]. This galaxy is an ideal candidate for this study because it has both circumnuclear star formation (Regan & Mulchaey 1999; Storchi-Bergmann et al. 2001; Sosa-Brito et al. 2001; Wold & Galliano 2006a) and a nuclear outflow observed by Morris et al. (1985) using the TAURUS Fabry–Perot spectrome-

ter. The outflows observed in the [O III] emission line are oriented approximately perpendicular to the Galactic plane, with velocities of up to $-100 \, km \, s^{-1}$, and are co-spatial with an ionization cone observed in an [O III] λ5007 narrow-band image (Storchi-Bergmann & Bonatto 1991).

Besides mapping the [O III] outflow, Morris et al. (1985) also reported the presence of a kpc-scale rotating disc in the plane of the galaxy, observed in Hα. Wold & Galliano (2006a) have studied the star formation in the circumnuclear disc using [Ne II]12.8 μm narrow-band images, and report the presence of embedded star clusters claiming that there are no counterparts detected at optical or near-IR wavelengths. They calculate the mass of the SMBH as $5.5 \times 10^7 \, M_\odot$ using high-resolution mid-IR spectroscopy.

We use *K*-band spectroscopic observations obtained with the integral field unit (IFU) of the Gemini near-infrared spectrograph (GNIRS) to map the stellar and gaseous flux distributions and kinematics of the inner few hundred parsec of NGC 7582. The *K*-band spectra allow the mapping of the stellar kinematics via the CO λ2.3 μm absorption feature, the ionized gas flux distribution and kinematics via the Brγ emission line and the molecular gas flux distribution and kinematics via the H_2 emission lines. This paper is organized as follows: in Section 2, we describe the observations and data reduction. In Section 3, we present the two-dimensional flux distributions and kinematics for both the emitting gas and stars. The results are discussed in Section 4, and in Section 5 we present our conclusions.

2 OBSERVATIONS AND DATA REDUCTION

The data were obtained at the Gemini South Telescope with the GNIRS IFU (Elias et al. 1998; Allington-Smith et al. 2006, 2007) in 2005 November 10 as part of program GS-2005B-Q-65, and comprise four individual exposures of 900 s centred at λ = 2.24 μm. The 111 1mm⁻¹ grating with the Short Blue Camera (0.15 arcsec pixel⁻¹) was used, resulting in a nominal resolving power of $R = 5900$. The GNIRS IFU has a rectangular field of view, of approximately 3.2×4.8 arcsec², divided into 21 slices. At the detector, the slices are divided along their length into 0.15 arcsec² IFU elements. The major axis of the IFU was oriented along position angle PA = 203°, in order to partially cover the ionization cone observed in the [O III]λ5007 narrow-band image by Storchi-Bergmann & Bonatto (1991). Two sets of observations were obtained, one centred at 1.2 arcsec from the nucleus along PA = 23° and the another centred at 0.75 arcsec from the nucleus along PA = 203°, the small offset being required to fill in the gaps between the slices. The observing procedure followed the standard object–sky–sky–object dither sequence, with off-source sky positions since the target is extended. Conditions during the observations were stable and clear, with an image quality in *K* band, in the range 0.45–0.55 arcsec, as obtained for the full width at half-maximum (FWHM) of the stellar profiles. The resulting spectral resolution, measured from the FWHM or the emission lines of the arc calibrations, is ≈2.9 Å.

The data reduction was accomplished using tasks in the GEMINI.GNIRS IRAF package as well as generic IRAF tasks. The reduction procedure included trimming of the images, flat-fielding, sky subtraction, wavelength calibration and *s*-distortion correction. The telluric bands were removed and the frames flux calibrated by interpolating a blackbody function to the spectrum of the telluric standard star, observed immediately after the galaxy. The final IFU datacube contains 840 spectra covering the spectral range from 2.14 to 2.33 μm, each spectrum corresponding to an angular coverage of

0.15×0.15 arcsec^2, which translates to 16×16 pc^2 at the galaxy. The total observed field of view 6.3×3.0 arcsec^2 (obtained by mosaicing the two set of observations) corresponds to a region of projected dimensions 660×315 pc at the galaxy.

3 RESULTS

In the top left-hand panel of Fig. 1, we present a large-scale optical *R*-band image of NGC 7582 from Hameed & Devereux (1999), obtained with the Cerro Tololo Inter-American Observatory (CTIO) 1.5 m telescope. The top right-hand panel presents a continuum image observed with the *HST* Wide Field Planetary Camera 2 (WFPC2) using the filter F606W obtained from the *HST* archive (program 8597 – PI: Regan, M.). We have overlaid on the *HST* image the contours (in green) of the narrow-band [O III] λ5007 image from Storchi-Bergmann & Bonatto (1991), which maps the ionization cone. The central rectangle shows the field of view of the GNIRS IFU observations, which covers only a small fraction of the ionization cone observed in [O III]. In the bottom right-hand panel, we present a Brγ flux distribution image reconstructed from the GNIRS IFU datacube, where we have marked, in magenta, the star clusters found by Wold & Galliano (2006a). These clusters

delineate an elongated ring of the recent star formation, with a semimajor axis of ≈1.7 arcsec, which was almost entirely covered by our observations.

In the bottom left-hand panel, we show three characteristic IFU spectra obtained within circular apertures of 0.4 arcsec radius: the nuclear spectrum – centred on the location corresponding to the peak flux in the continuum (position N in the Brγ intensity map), and spectra from two locations at 1.7 arcsec NW (position A) and at 1.7 arcsec SE of the nucleus (position B), located in the star-forming ring. The spectra of the latter regions present emission lines of Brγ λ2.1661 μm, H$_2$ λ2.2235 μm and H$_2$ λ2.2477 μm, used to map the gaseous kinematics and flux distributions, and the stellar absorption band of ^{12}CO (2,0) λ2.2935 μm, used to obtain the stellar kinematics. The nuclear spectrum is redder than those from the ring, with a flux in the continuum 10 to 15 times higher than in the ring, and shows a narrow Brγ emission line, on the top of what seems to be a broad component of the line.

3.1 Emission-line flux distributions

Flux distributions in the emission lines were obtained directly from the datacube by integrating the flux under each emission-line profile
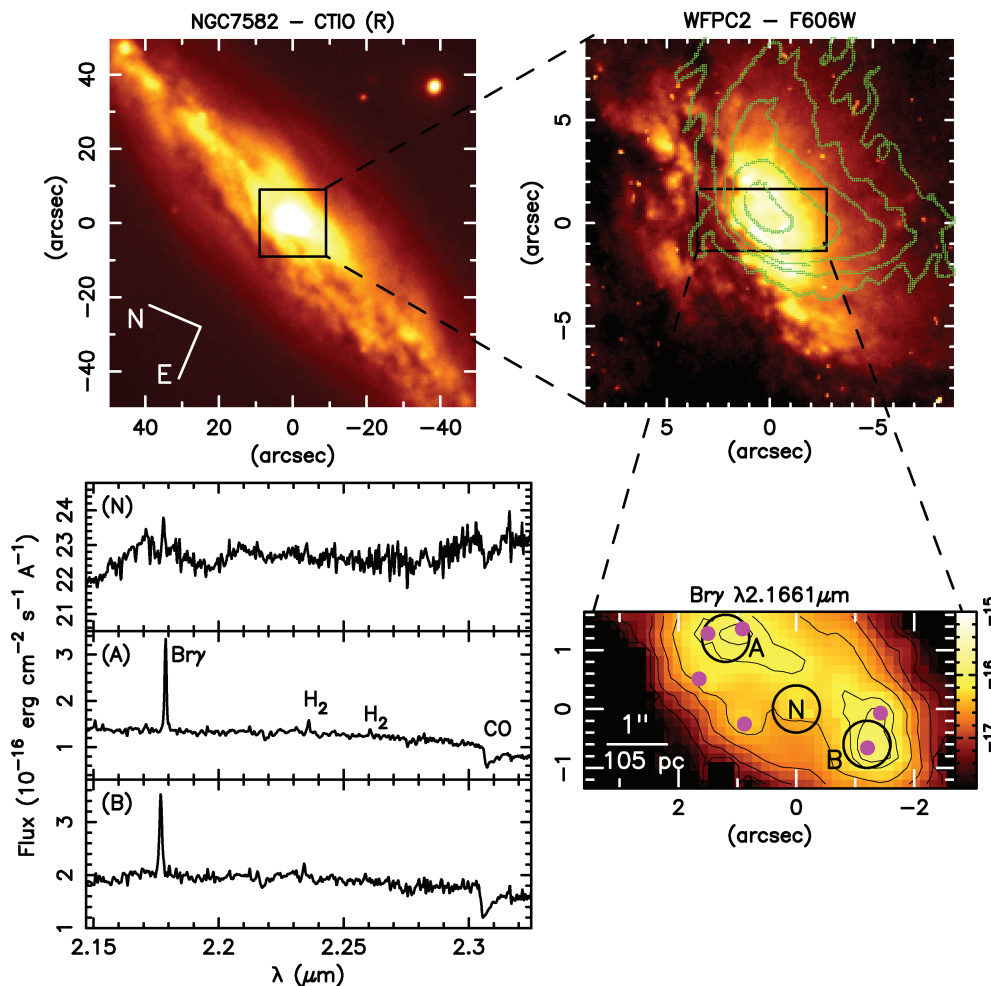

Figure 1. Top left-hand panel: large-scale image of NGC 7582 from Hameed & Devereux (1999). Top right-hand panel: *HST* WFPC2 image for the central region of NGC 7582. The green contours are for the [O III] emission form Storchi-Bergmann et al. (1999). Bottom right-hand panel: Brγ flux map reconstructed from the GNIRS IFU spectroscopy. Bottom left-hand panel: spectra extracted for a circular aperture of 0.4 arcsec radius centred at the positions N, A and B marked at the bottom right-hand panel with the emission lines and CO absorption bandhead identified.

and subtracting the continuum contribution using images obtained in windows adjacent to the emission line.

We have also adjusted Gaussian profiles to the emission lines in order to measure the gas radial velocity (from the central wavelength of the line) and the velocity dispersion (from the width of the line). The fitting of each emission-line profile was obtained using the SPLOT IRAF task, and resulted also in an integrated flux for each line, from which we also obtained flux distributions. A comparison of the flux distributions obtained via the fitting of Gaussians to the flux distributions obtained directly from the datacube showed that although both flux distributions agree with each other within the uncertainties, the ones obtained via Gaussian fitting are less noisy away from the nucleus. These flux distributions are shown in Fig. 2 for the Brγ (top panel) and H$_2$ $\lambda2.2235\,\mu$m (middle panel) emission lines with mean uncertainties of 6 and 11 per cent, respectively. The Brγ emission is extended along the major axis of the galaxy (PA $\approx 165°$) and shows flux enhancements in an arc-shaped struc-

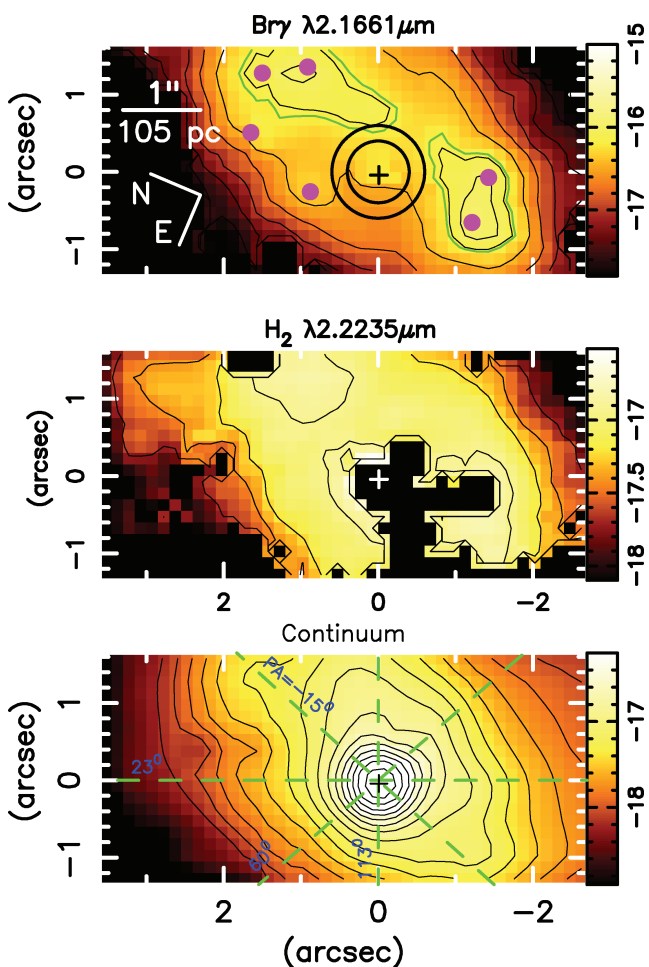**Figure 2.** Two-dimensional flux maps for the Brγ (top panel), and H$_2$ $\lambda2.2235\,\mu$m (middle panel) emission lines with mean uncertainties of 6 and 11 per cent, respectively, and reconstructed image for the 2.17 μm continuum emission (bottom panel). The black contours are iso-intensity curves, and the green contours in the Brγ flux map delimit regions where the line flux per pixel is higher than 50 per cent of the peak flux in the region. The magenta filled circles indicate the position of the embedded star clusters observed by Wold & Galliano (2006a). The black circles surrounding the nucleus in the Brγ flux map represent the apertures used to extract the spectra shown in Fig. 8 and the green dashed lines show the orientation of the pseudo-slits used to construct one-dimensional cuts shown in Fig. 10.

ture which approximately traces the star clusters observed by Wold & Galliano (2006a), shown again by the magenta circles. Two strong Brγ emission peaks in the ring are located at ≈1.7 arcsec NW and ≈1.7 arcsec SE of the nucleus, and are encircled by the green contours in Fig. 2, which correspond to the limits within which the flux in each pixel is higher than 50 per cent of the peak flux in the region. We note that each of our encircled regions includes two of the clusters identified by Wold & Galliano (2006a). While the Brγ flux distribution shows intensity variations and enhancements in the position corresponding to the star clusters, mapping the ring of star formation, the H$_2$ flux distribution (middle panel of Fig. 2) is more uniform throughout the nuclear region, showing no enhancements at the star clusters. The black regions correspond to pixels for which the signal-to-noise (S/N) ratio was too low to allow a reliable measurement of the emission line.

The bottom panel of Fig. 2 shows the 2.17 μm continuum image obtained from interpolation between two continuum windows adjacent to the Brγ profile. The iso-intensity contours in the continuum image are asymmetric, being more extended to the W–SW than to the E–NE, as expected, due to the strong dust absorption observed in optical images, in good agreement with the 1.6 μm continuum image presented by Wold & Galliano (2006a).

3.2 Stellar kinematics

In order to obtain the stellar line-of-sight velocity distribution (LOSVD), we fitted the ^{12}CO(2,0) stellar absorption bandhead at 2.2935 μm in the K-band spectra using the penalized Pixel-Fitting (pPXF) method of Cappellari & Emsellem (2004). The algorithm finds the best fit to a galaxy spectrum by convolving template stellar spectra with a given LOSVD. This procedure outputs the stellar radial velocity, velocity dispersion and higher order Gauss–Hermite moments for each spectrum fitted. The pPXF method allows the use of several stellar templates, and also to vary the relative contribution of the different templates to obtain the best fit, thus minimizing the problem of template mismatch. For this study, we have selected as template spectra those of the Gemini spectroscopic library of late spectral type stars observed with the GNIRS IFU using the grating 111$\,$l$\,$mm^{-1} in the K band (Winge, Riffel & Storchi-Bergmann 2007). In Riffel et al. (2008), we describe some properties of this library and discuss the problem of template mismatch using the CO absorption bandheads with the pPXF method.

In Fig. 3, we show the resulting fit for positions A (top panel) and B (bottom panel) marked in Fig. 1. For the regions where the S/N ratio was lower than ≈30, we replaced the spectrum of each single pixel by an average including the nine nearest pixels. Even adopting this procedure, we could obtain measurements of the stellar kinematics only for the central 4.8×3.0 arcsec^2 region, as the S/N ratio of the spectra close to the borders of the IFU field becomes too low to obtain a reliable fit. For this same reason, we could not also obtain stellar kinematic measurements very close to the nucleus (radius < 0.3 arcsec), as the CO bandhead feature becomes diluted by dust and line emission.

In Fig. 4, we present two-dimensional maps of the stellar kinematics. Black pixels in this figure correspond to the masked regions where we did not obtain a reliable fit. The central cross marks the position of the nucleus, defined as the locus of the peak of the K-band continuum and the dashed line shows the PA = 165°, which is the position angle of the major axis of the galaxy (Morris et al. 1985). The top left-hand panel of Fig. 4 shows the stellar radial velocity field, from which we subtracted the systemic velocity of
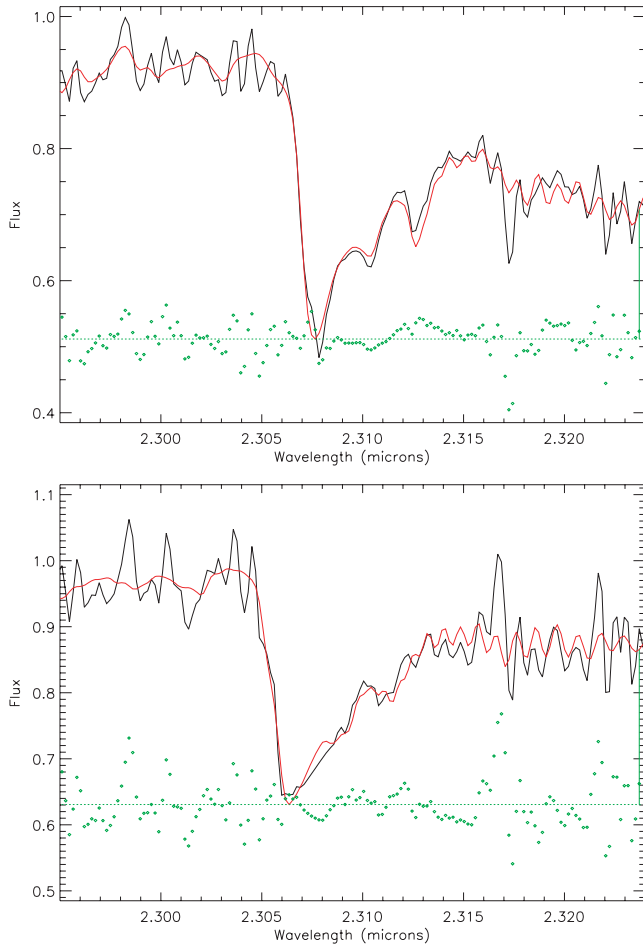
Figure 3. Fits of the stellar kinematics for the positions A (top panel) and B (bottom panel) shown in Fig. 1. The observed spectra are shown in black, the fitted template in red and the residuals in green.

the galaxy listed in the HYPERLEDA[1] data base – $V_s = 1605$ km s^{-1} (relative the local standard of rest), which agrees with our value for the nuclear region. The mean uncertainty in the radial velocity is ≈ 15 km s^{-1}. The radial velocity field shows blueshifts to the SE and redshifts to the NW, suggesting rotation, although with the kinematical centre displaced from the peak of the continuum emission. The velocity field has an amplitude of ≈ 200 km s^{-1} (from -100 to 100 km s^{-1}) and seems not to be symmetric relative to the nucleus, with the highest blueshifts to the S–SW being reached closer to the nucleus than the highest redshifts to the N–NW. A one-dimensional cut along the galaxy major axis suggests that the turnover of the rotation curve to the S–SW is reached already at ≈ 100–150 pc from the nucleus, but the turnover to the N–NW seems to be beyond the border of the field (see Fig. 10).

In the top right-hand panel of Fig. 4, we present the stellar velocity dispersion (σ_*) map, with values ranging from 40 to 170 km s^{-1}, and mean uncertainties of ≈ 10 km s^{-1}. The highest values are observed to the E and S of the nucleus. A partial ring of low σ_* values (≈ 50 km s^{-1}) is observed at ≈ 1 arcsec from the nucleus, surrounding it from N to SW. The h_3 and h_4 Gauss–Hermite moment maps, which measure deviations of the LOSVD from a Gaussian distribution, are presented at the bottom panels of Fig. 4 and have mean

uncertainties of 0.03. The values of h_3 and h_4 are between -0.18 and 0.18, which are similar to typical values obtained for a large number of galaxies in similar analyses (Emsellem et al. 2004; Ganda et al. 2006).

3.3 Gas kinematics

In the left-hand panels of Fig. 5, we present the radial velocity fields obtained from the peak wavelengths of the Brγ and H$_2$ $\lambda 2.2235$ μm emission lines, with mean uncertainties of 6 and 9 km s^{-1}, respectively. The systemic velocity of the galaxy has been subtracted from all the emission-line velocity maps. The velocity field of the Brγ emitting gas is very similar to that of the H$_2$ emitting gas, being also similar to the stellar velocity field, with the S–SE side approaching and the N–NW side receding. The largest blueshifts are observed S of the nucleus reaching values of ≈ -170 km s^{-1}, while the largest redshifts reach smaller values of ≈ 100 km s^{-1} and are observed NW of the nucleus.

The gas velocity dispersion (σ) maps are shown in the right-hand panels of Fig. 5. Mean uncertainties are 7 km s^{-1} for Brγ and 10 km s^{-1} for H$_2$. The values were corrected for the instrumental broadening ($\sigma_{inst} \approx 18$ km s^{-1}), and range from $\sigma \approx 20$ to 90 km s^{-1} for Brγ and from $\sigma \approx 20$ to 70 km s^{-1} for H$_2$. The Brγ velocity dispersion shows regions of low values ($\sigma \approx 30$ km s^{-1}) to the N of the nucleus and higher values to the S–SE. The highest σ values observed in the H$_2$ line are located around the nucleus, and the lowest values in regions away from it.

3.4 Velocity slices

In order to better map the gaseous kinematics, and as our data have a relatively high-spectral resolving power, we could 'slice' the line profiles in a sequence of velocity channels. Our goal is to better sample the gas kinematics over the whole velocity distribution, including the emission-line wings (see Gerssen et al. 2006; Riffel et al. 2006, 2008). The flux distributions in the velocity slices were obtained after the subtraction of the continuum contribution determined as the average of the flux from both sides of the emission lines. Each slice corresponds to a velocity bin of ≈ 50 km s^{-1} (two spectral pixels) and the resulting flux distributions are shown in Figs 6 and 7. In these figures, the flux levels are presented in logarithmic units, and the slices trace the gas from negative (blueshifted, top left-hand panel) to positive (redshifted, bottom right-hand panel) velocities relative to the systemic velocity. For the Brγ emitting gas, the highest blueshifts of ≈ -360 km s^{-1} are observed at ≈ 1 arcsec SW of the nucleus, while the highest redshifts of ≈ 260 km s^{-1} are observed at ≈ 2 arcsec NW of the nucleus. For the H$_2$ emitting gas, the highest blueshifts reach ≈ -300 km s^{-1} and the highest redshifts ≈ 160 km s^{-1}, observed approximately at the same locations as for the Brγ emission. While the highest blueshifts are observed displaced from the major axis, in the velocity range from ≈ -200 to 200 km s^{-1}, the emission peak moves from S–SE to N–NW essentially parallel to the major axis, suggesting that, for this range of velocities, the emission is dominated by gas rotating in the plane of the galaxy.

4 DISCUSSION

4.1 The nuclear spectrum

The flux distribution in the continuum shows an unresolved source at the nucleus (whose location we assume to coincide with the peak of the flux distribution). In order to isolate the spectrum of the nuclear
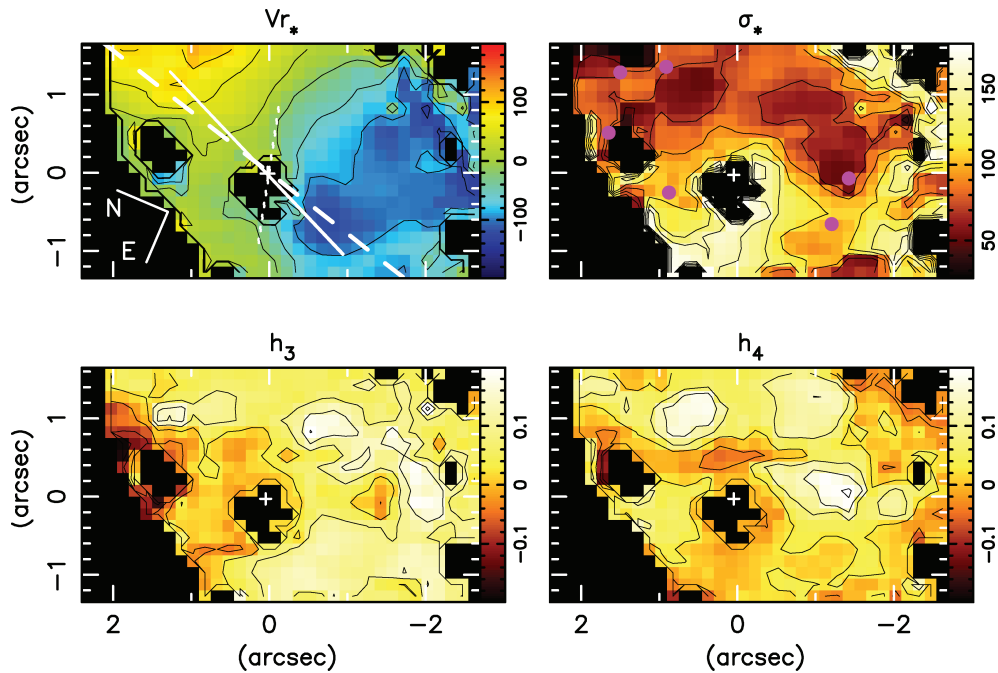
Figure 4. Two-dimensional maps of the stellar kinematics. Top left-hand panel: radial velocities with mean uncertainties of 15 km s^{-1}. Top right-hand panel: velocity dispersions with uncertainties of 10 km s^{-1}. Bottom panel: h_3 and h_4 Gauss–Hermite moments with uncertainties of 0.03. The dashed line represents the PA of the major axis of the galaxy, while the dotted and solid lines show the orientation and extent of the nuclear bar and nuclear spiral arms, respectively, observed by Acosta-Pulido et al. (2003). The cross marks the position of the nucleus and the magenta filled circles indicate the position of the star clusters observed by Wold & Galliano (2006a). The orientation is shown in the top left-hand panel.
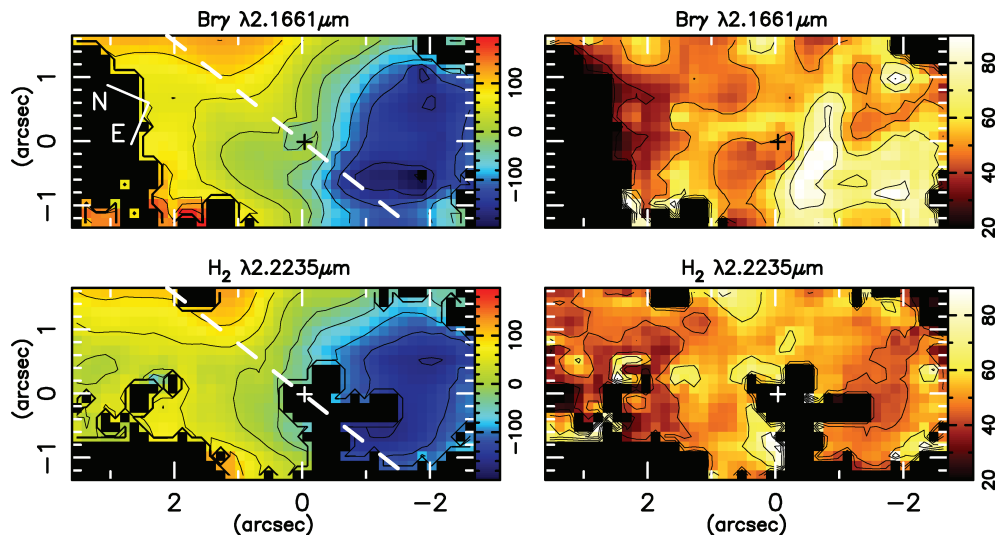

Figure 5. Left-hand panel: radial velocity maps for the Brγ (top panel) and H$_2$ $\lambda 2.2235$ μm (bottom panel) emitting gas, with mean uncertainties of 6 and 9 km s^{-1}, respectively. Right-hand panel: velocity dispersion maps for the same emission lines with mean uncertainties of 7 km s^{-1} for Brγ, and 10 km s^{-1} for H$_2$. The dashed line represents the orientation of the major axis of the galaxy.

source, we have extracted its spectrum within an aperture of radius 0.4 arcsec, which corresponds to the radial distance where the point source profile decreases to one-third of its peak value. In order to subtract the underlying stellar contribution to the nuclear flux, we have extracted a spectrum within a ring with inner and outer radii of 0.4 and 0.6 arcsec, respectively, surrounding the nuclear aperture. We show the apertures corresponding to the nuclear and extranuclear spectra as circles in the top panel of Fig. 2. This choice of apertures was dictated by the need to isolate the nuclear spectrum from that

of the circumnuclear ring of star formation. Larger apertures for the nuclear and the extranuclear spectra would include contribution from the star-forming ring.

The resulting nuclear and extranuclear spectra are shown in Fig. 8 (top and bottom spectra). In the same figure, we also show the difference between them (middle spectrum) after scaling the circumnuclear spectrum to the flux it would have if obtained through the same aperture as that of the nuclear spectrum. We note that the circumnuclear spectrum does not differ much from those of
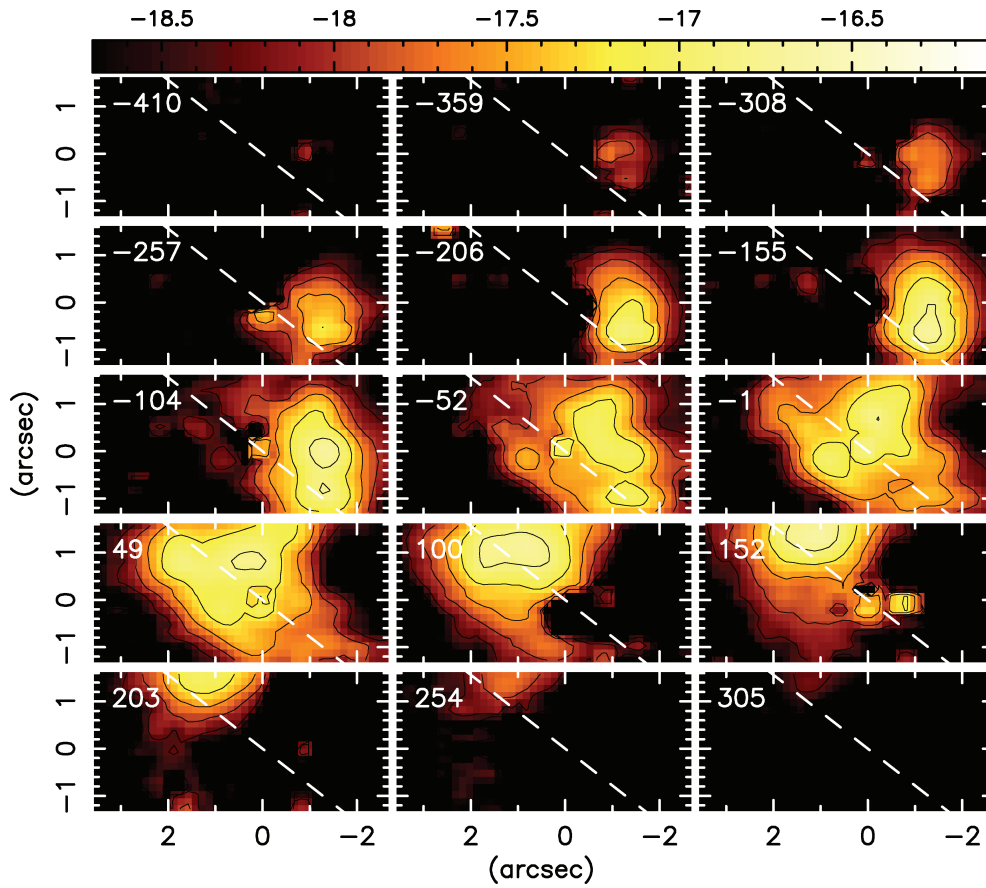
Figure 6. Velocity slices along the Brγ emission-line profile in steps of ≈50 km s⁻¹. The dashed lines represent the orientation of the major axis of the galaxy and the velocity corresponding to the centre of each bin is shown at the top left-hand corner of the corresponding panel.
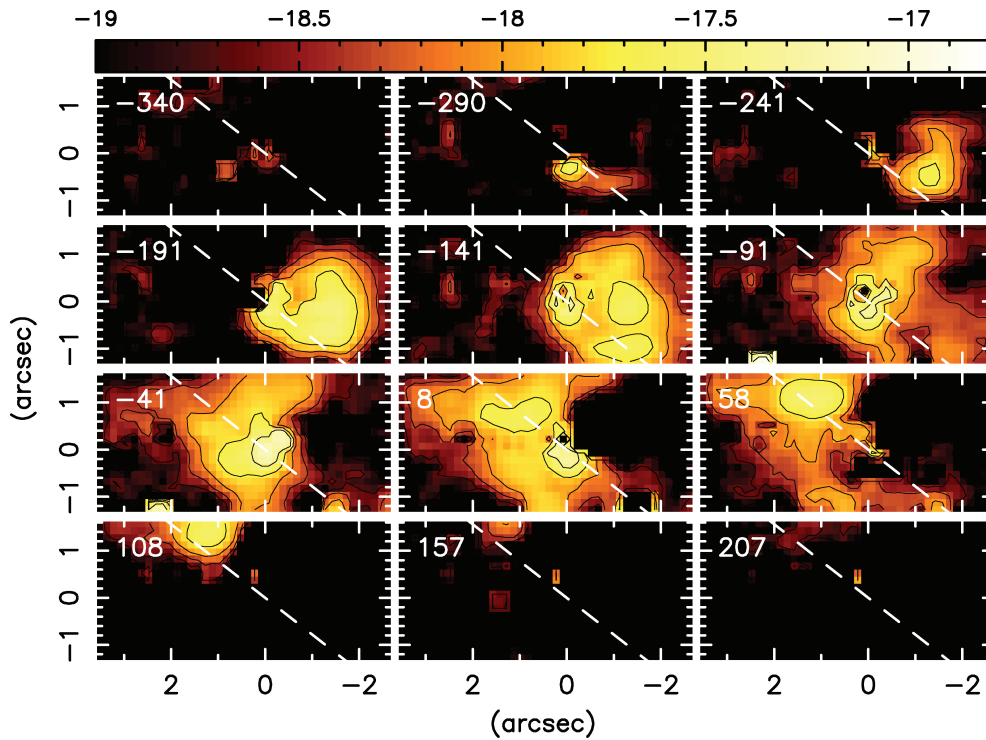
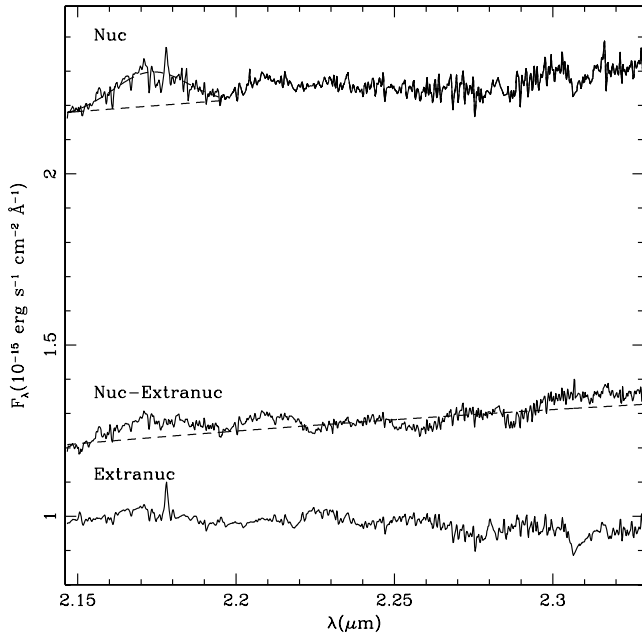**Figure 7.** Same as Fig. 6 for the H₂ λ2.2235 μm emission-line profile.

Figure 8. Nuclear spectrum of NGC 7582 for a circular aperture of 0.8 arcsec diameter (top spectrum), extranuclear spectrum for a ring with inner radius of 0.4 arcsec and outer radius of 0.6 arcsec from the nucleus (bottom spectrum) and the difference between the two (middle spectrum). The extranuclear spectrum was scaled by the ratio between the areas of the nuclear and extranuclear apertures.

the star-forming regions A and B, suggesting that recent star formation is occurring also inside the ring. This is supported by previous studies of the stellar population in the optical (Storchi-Bergmann et al. 2001) and near-IR (Davies et al. 2005).

The nuclear spectrum seems to present both a narrow and a broad component in the Brγ emission line. The fit of a Gaussian to the broad component, as illustrated in the top spectrum of Fig. 8, gives a FWHM ≈ 3900 km s^{-1}, with the centre of the line blueshifted by ≈ 650 km s^{-1} relative to the narrow component. The presence of a broad component in Brγ, with FWHM ≈ 4000 km s^{-1}, has been previously reported by Davies et al. (2005), in long-slit observations obtained with the Very Large Telescope. A broad component, observed in Hα, was also reported by Aretxaga et al. (1999), although this component seems to have been produced by a transient event. These authors noted the appearance and subsequent fading of the broad Hα component as well as other optical emission lines and proposed three possible scenarios for its origin: capture and disruption of a star by a SMBH, a reddening change in a dusty torus surrounding the nucleus and a Type IIn supernova exploding in a compact starburst.

The nuclear spectrum is redder than the extranuclear one, and the subtraction of the stellar contribution does seem to have eliminated the stellar 2.3 μm CO absorption, clearly observed prior to the subtraction. The resulting spectrum shows a red continuum similar to those of other red unresolved components observed in other AGN and attributed to emission from hot dust, possibly distributed in a toroidal structure around the SMBH, with temperature close to the dust sublimation temperature (Barvainis 1987; Marco & Alloin 1998, 2000; Rodríguez-Ardila, Contini & Viegas 2005b; Rodríguez-Ardila & Mazzalay 2006). Under the assumption that the red unresolved component is indeed due to emission by dust,

we have derived its temperature and mass, by fitting a blackbody function to its spectrum. The resulting fit is shown as a dashed line in the middle spectrum of Fig. 8, corresponding to a temperature $T \approx 1050 \pm 140$ K, for which the maximum of the blackbody curve is reached at ≈ 2.76 μm.

We have estimated the mass of the hot dust producing the emission in the unresolved component using the formalism of Barvainis (1987), for dust composed by grains of graphite. The IR spectral luminosity of each dust grain, in erg s^{-1} Hz^{-1}, can be written as

$$L_{\nu,\mathrm{ir}}^{\mathrm{gr}} = 4\pi^2 a^2 Q_\nu B_\nu(T_{\mathrm{gr}}), \tag{1}$$

where a is the grain radius, Q_ν is its absorption efficiency and $B_\nu(T_{\mathrm{gr}})$ is its spectral distribution assumed to be a Planck function for a temperature T_{gr}.

The total number of graphite grains can be obtained from

$$N_{\mathrm{HD}} \approx \frac{L_{\mathrm{ir}}^{\mathrm{HD}}}{L_{\mathrm{ir}}^{\mathrm{gr}}}, \tag{2}$$

where $L_{\mathrm{ir}}^{\mathrm{HD}}$ is the total luminosity of the hot dust, obtained by integrating the flux under the function fitted to the nuclear–extranuclear spectrum and adopting a distance to NGC 7582 of $d = 21.6$ Mpc. In order to obtain $L_{\mathrm{ir}}^{\mathrm{gr}}$, we have adopted $T_{\mathrm{gr}} = 1050$ K, as derived above, $a = 0.05$ μm and $Q_\nu = 1.4 \times 10^{-24}\nu^{1.6}$ (for ν in Hz) as in Barvainis (1987). Finally, we can obtain the total mass of the emitting dust as

$$M_{\mathrm{HD}} \approx \frac{4\pi}{3} a^3 N_{\mathrm{HD}} \rho_{\mathrm{gr}} \tag{3}$$

Adopting $\rho_{\mathrm{gr}} = 2.26$ g cm^{-3} for the graphite density (Granato & Danese 1994), we obtain $M_{\mathrm{HD}} \approx 2.8 \times 10^{-3}$ M$_\odot$. In Table 1, we compare this dust mass with masses of hot dust obtained for other AGN in previous studies. The hot dust mass in NGC 7582 is similar to those obtained for Mrk 766, NGC 1068 and NGC 3783, while it is smaller than the values for Mrk 1239, NGC 7469 and Fairall 9, and higher than those derived for NGC 1566 and NGC 4593.

For Mrk 1239 (Rodríguez-Ardila & Mazzalay 2006) and Mrk 766 (Rodríguez-Ardila et al. 2005b), the dust mass values were derived from long-slit spectroscopy, with extraction apertures of the nuclear spectrum corresponding to more than 100 pc at the galaxies, while the spatial resolution of our data allows us to constrain the location of the hot dust as being within ≈ 25 pc from the nucleus. As pointed out above, the K-band excess is probably due to the emission of hot dust from a circumnuclear torus which may be located even closer to the SMBH. In the case of NGC 1097, for example, Storchi-Bergmann et al. (2005) have found a heavily obscured starburst closer than 9 pc from the nucleus, which could be located in the outskirts of the torus. In the case of NGC 1068, interferometric mid-IR observations constrained the hot dust emission to originate

Table 1. Masses of hot dust found in AGN.

Galaxy	M_{HD} (M$_\odot$)	Reference
NGC 7582	2.8×10^{-3}	This work
Mrk 1239	2.7×10^{-2}	Rodríguez-Ardila & Mazzalay (2006)
Mrk 766	2.1×10^{-3}	Rodríguez-Ardila et al. (2005b)
NGC 1068	1.1×10^{-3}	Marco & Alloin (2000)
NGC 7469	5.2×10^{-2}	Marco & Alloin (1998)
NGC 4593	5.0×10^{-4}	Santos-Lléo et al. (1995)
NGC 3783	2.5×10^{-3}	Glass (1992)
NGC 1566	7.0×10^{-4}	Baribaud et al. (1992)
Fairall 9	2.0×10^{-2}	Clavel, Wamsteker & Glass (1989)

much closer, in a region of approximately 1 pc diameter (Jaffe et al. 2004).

4.2 Circumnuclear star-forming regions

NGC 7582 is known to present a kpc-scale Hα emitting disc which harbours recent star formation plus heavy dust obscuration in the nuclear region (Morris et al. 1985; Regan & Mulchaey 1999; Storchi-Bergmann et al. 2001; Sosa-Brito et al. 2001; Wold & Galliano 2006a). The presence of dust to the NE is responsible for the asymmetric contours of the continuum flux map in the bottom panel of Fig. 2. The recent star formation in the dust-embedded clusters reported by Wold & Galliano (2006a) (shown as magenta circles in Fig. 2) is seen as enhancements in our Brγ image, delineating a ring of major axis of ≈3.5 arcsec and minor axis of ≈1.5 arcsec. This gives an axial ratio of $\frac{a}{b} \approx 2.3$, which is similar to the axial ratio of the galaxy ($\frac{a}{b} \approx 2.2^2$), suggesting that the star-forming ring is circular, with a radius of ≈190 pc and is located in the plane of the galaxy. As pointed out by Wold & Galliano (2006a), these star-forming clusters had not been previously seen neither in the optical nor in the near-IR. The near-IR IFU data from Sosa-Brito et al. (2001), although consistent with our results, does not have the necessary spatial resolution to resolve these clusters.

In our data alone, clear peaks in the Brγ flux distribution are located in the ring at 1.7 arcsec NW and 1.7 arcsec SE of the nucleus, and are encircled by the green contours in Fig. 2, which comprise the pixels with fluxes higher than 50 per cent of the peak flux. We will refer to each of these two regions – whose physical boundaries we define as corresponding to the green contours – as circumnuclear star-forming regions (CNSFRs), and will use our data for these regions to characterize the star formation in the circumnuclear ring. From the locations of the star clusters found by Wold & Galliano (2006a), it can be seen that each of these CNSFRS corresponds to two star clusters, thus we should bear in mind that the parameters we obtain for these regions correspond to two star clusters instead of one.

Following Riffel et al. (2008), we can estimate the mass of ionized hydrogen in each CNSFR as

$$\left(\frac{M_{\mathrm{H\,II}}}{\mathrm{M}_\odot}\right) = 2.88 \times 10^{17} \left(\frac{F_{\mathrm{Br}\gamma}}{\mathrm{erg\,s^{-1}\,cm^{-2}}}\right)\left(\frac{d}{\mathrm{Mpc}}\right)^2, \qquad (4)$$

where $F_{\mathrm{Br}\gamma}$ is the line flux, d is the distance of the galaxy and we have assumed an electron temperature $T = 10^4$ K and electron density $N_{\mathrm{e}} = 100$ cm^{-3} for the CNSFRs.

We can also obtain the emission rate of ionizing photons for each CNSFR using (Osterbrock 1989)

$$Q[H^+] = \frac{\alpha_{\mathrm{B}}\,L_{\mathrm{H}\alpha}}{\alpha_{\mathrm{H}\alpha}^{\mathrm{eff}}\,h\nu_{\mathrm{H}\alpha}}, \qquad (5)$$

where α_{B} is the hydrogen recombination coefficient to all energy levels above the ground level, $\alpha_{\mathrm{H}\alpha}^{\mathrm{eff}}$ is the effective recombination coefficient for Hα, h is the Planck's constant and $\nu_{\mathrm{H}\alpha}$ is the frequency of the Hα line. Using $\alpha_{\mathrm{B}} = 2.59 \times 10^{-13}$ cm^3 s^{-1}, $\alpha_{\mathrm{H}\alpha}^{\mathrm{eff}} = 1.17 \times 10^{-17}$ cm^3 s^{-1} and $L_{\mathrm{H}\alpha}/L_{\mathrm{Br}\gamma} = 102.05$ for case B recombination assuming an electronic temperature $T_{\mathrm{e}} = 10^4$ K (Osterbrock 1989), we obtain

$$\left(\frac{Q[H^+]}{\mathrm{s^{-1}}}\right) = 7.47 \times 10^{13} \left(\frac{L_{\mathrm{Br}\gamma}}{\mathrm{erg\,s^{-1}}}\right). \qquad (6)$$

Finally, we can also obtain the SFR using (Kennicutt 1998)

$$\left(\frac{\mathrm{SFR}}{\mathrm{M}_\odot\mathrm{yr^{-1}}}\right) = 8.2 \times 10^{-40} \left(\frac{L_{\mathrm{Br}\gamma}}{\mathrm{erg\,s^{-1}}}\right), \qquad (7)$$

under the same assumptions adopted to derive equation (6).

As there is a considerable obscuration in the nuclear region of NGC 7582, the emission-line fluxes used in the above equations have been corrected for reddening. We have used $E(B - V) = 0.6$, obtained by Schmitt, Storchi-Bergmann & Cid Fernandes (1999) in a spectrum extracted within an aperture of 2×2 arcsec^2, adopting the extinction law of Cardelli, Clayton & Mathis (1989).

Besides calculating the above quantities for the two CNSFRs, we have also calculated them for the nucleus and for the complete ring of star formation, as follows. In order to obtain the emission rate of ionizing photons for the nucleus, we integrated the Brγ emission-line flux within a circular aperture of 0.4 arcsec plus that emitted by the outflowing gas, under the assumption that the outflowing gas is ionized by the active nucleus. The flux in the outflowing gas was estimated as the sum of the fluxes in the velocity slices with $|v| > 200$ km s^{-1}. In this manner, we obtain only a lower limit for the rate of ionizing photons emitted by the nucleus, as our field of view covers only a very small portion of the outflow, as discussed in Section 3. An upper limit can be obtained under the assumption that the total flux in the outflow is the one observed times the ratio between the total area covered by the outflow (estimated from the [O III] image) and that covered by our observations, which is ≈5. Considering that there should be a counterpart outflow to the opposite side of the galaxy plane, probably hidden by the dust in the plane, the Brγ flux in the outflow may be ≈10 times the one measured from our data. The Brγ flux of the star-forming ring was obtained by integrating its value over the whole IFU field and subtracting the contribution of the nuclear flux plus that of the outflowing gas.

Table 2 presents the results of the above calculations, together with the area used in the integrations and the Brγ emission-line luminosities corrected for reddening. For the nucleus, we list both the lower limit (including only the contribution of the observed outflow) and the upper limit (including the contribution of the total estimated outflow). We also list the equivalent widths of the Brγ emission line.

Table 2 shows that the Brγ flux in inner ≈400 pc of NGC 7582 is dominated by emission from the circumnuclear star-forming ring, which ranges from 4 to 13 times that of the nucleus plus outflow. The Brγ fluxes of the two CNSFRs contribute with 50 per cent of the total emission from the star formation ring.

The emission rates of ionizing photons obtained for the two CNSFRs are in good agreement with values obtained for CNSFRs in other galaxies (e.g. Galliano & Alloin 2008; Hägele et al. 2007), as well as with rates derived for NGC 7582 in the mid-IR (Wold & Galliano 2006a). Such rates correspond to about 1000 O6 stars in each CNSFR (Osterbrock 1989). Considering that each CNSFR actually corresponds to two clusters, then this would correspond to ≈500 O stars per cluster.

The SFRs for the CNSFRs of SFR ≈ 0.23–0.28 M$_\odot$ yr^{-1} characterize a moderate star-forming regime, and are in good agreement with the values derived by Shi, Gu & Peng (2006) for a sample of 385 CNSFRs in galaxies covering a range of Hubble types.

4.2.1 Age of the CNSFRs

We can also use our data to estimate the age of the CNSFRs, applying the method described by Dors et al. (2008), which consists of

---

^{2} From HYPERLEDA data base (http://leda.univ-lyon1.fr).

Table 2. Physical parameters obtained for the CNSFRs in NGC 7582.

Parameter	1.7 arcsec NW	1.7 arcsec SE	Nucleus$^{(nuc+ulo)a}_{(nuc+llo)b}$	Ring
Area (arcsec^2)	1.48	1.15	0.5	18.4
$\log L(Br\gamma)$ (erg s^{-1})	38.53 ± 0.03	38.45 ± 0.03	$37.81^{(38.52)}_{(37.96)} \pm 0.04$	39.09 ± 0.03
$\log Q[H^+]\,(s^{-1})$	52.40 ± 0.03	52.32 ± 0.03	$51.68^{(52.39)}_{(51.83)} \pm 0.04$	52.96 ± 0.03
SFR (M$_\odot$ yr^{-1})	0.28 ± 0.02	0.23 ± 0.02	–	1.01 ± 0.07
EW(Brγ) (Å)	14.7 ± 1.4	13.6 ± 1.3	0.8 ± 0.1	7.1 ± 0.6
M_{HII} (10^5 M$_\odot$)	8.2 ± 0.6	6.8 ± 0.5	$1.5^{(8.2)}_{(2.2)} \pm 0.2$	29.4 ± 2.0

^{a}Nucleus plus upper limit for the outflowing gas component.
^{b}Nucleus plus lower limit for the outflowing gas component.
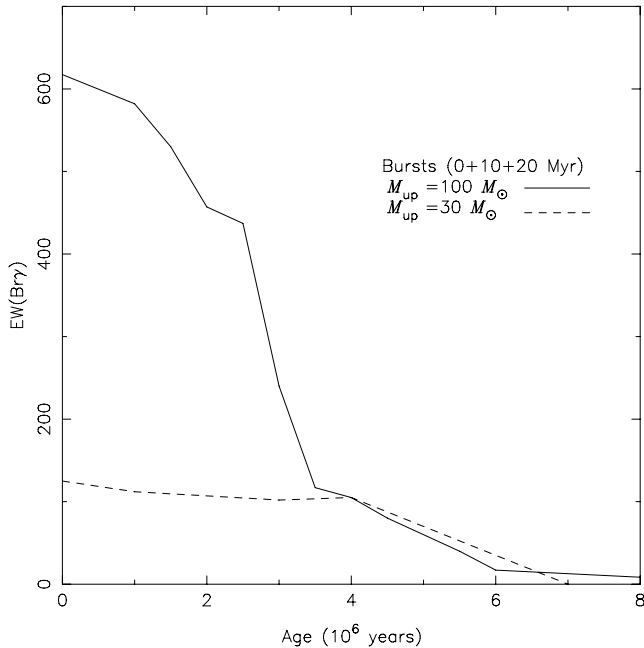
Figure 9. Equivalent width of Brγ as predicted by evolutionary photoionization models (Dors et al. 2008).

comparing the observed values of EW(Brγ) to those predicted by evolutionary photoionization models. As stressed by those authors, the real age of the CNSFRs can only be obtained if the contributions from both the underlying bulge and older stars in the CNSFRs are taken into account.

In order to obtain the contribution of the underlying bulge, we used aperture photometry in the continuum image (Fig. 2) to measure both the flux of the CNSFRs continua and that of the bulge in the surrounding regions. We find a bulge contribution of ≈50 per cent of the total flux at both CNSFRs, and thus the value of EW(Brγ) increases from 15 to 30 Å after this correction.

The presence in the CNSFRs of stars formed in previous bursts of star formation is supported by the work of Schmitt et al. (1999), who found a large spread of age in the circumnuclear star-forming regions. In order to take this effect into account, we apply the same approach as Dors et al. (2008), representing the CNSFR stellar content by three bursts of star formation, with ages of 0.1, 10 and 20 Myr, and considering two values for the upper limit in stellar mass ($M_{up} = 100$ and 30 M$_\odot$). The resulting evolutionary behaviour of EW(Brγ) is illustrated in Fig. 9. For a value of EW(Brγ)≈30 Å, we obtain an age of ≈5.0 Myr, which is similar to the values

found for the CNSFRs in NGC 6951 and NGC 1097 by Dors et al. (2008).

4.3 Stellar kinematics

As observed in Fig. 4, the stellar velocity field seems to be dominated by rotation. We have thus tried to fit the stellar velocities by a model of circular orbits in a plane subject to a Plummer potential, which successfully reproduced the stellar kinematics of the central regions of other Seyfert galaxies in previous studies (e.g. Barbosa et al. 2006; Riffel et al. 2008). Nevertheless, in the case of NGC 7582 this model fails, as the residuals are too large everywhere. The kinematic centre of the rotation in Fig. 4 seems to be displaced from the nucleus by ≈0.5 arcsec NW (≈50 pc at the galaxy), an effect which can also be observed in one-dimensional cuts of the velocity field shown in Fig. 10. This is an interesting result which should be further investigated. Could this be the kinematic centre of
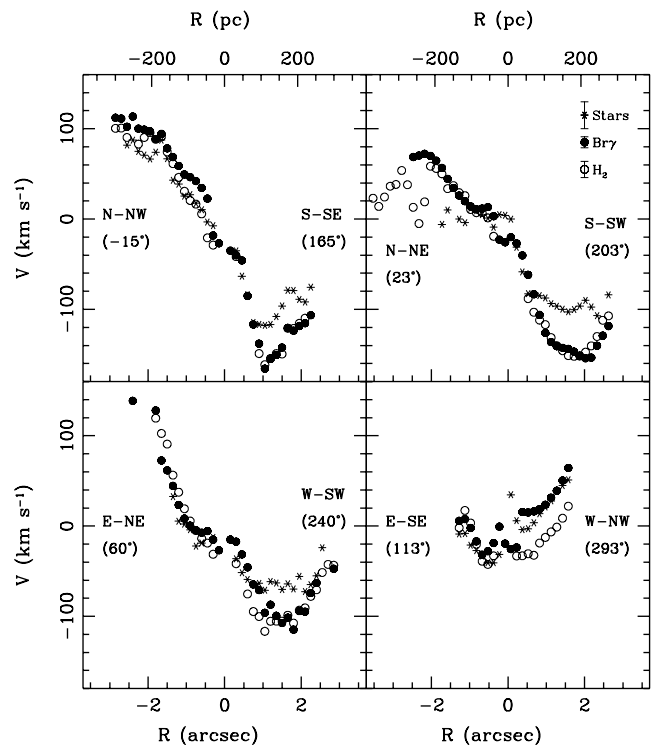
Figure 10. One-dimensional cuts of the gaseous (black circles and crosses) and stellar (open circles) radial velocities obtained along the PAs −15–165°, 23–203°, 60–240° and 113–293° for a pseudo-slit of 0.45 arcsec width.

the galaxy? If this is the case, then the peak flux of the IR continuum would not correspond to the centre of the galaxy but instead to the location of the SMBH (the unresolved red source), and the ring of star formation would be centred on the SMBH instead of the galaxy centre. We believe this is unlikely, as the radius of influence of the SMBH is much smaller than the radius of the ring, and thus one would expect that the ring would be centred on the galaxy nucleus. Our field of view is too small for us to reach a firm conclusion, but one possibility is that the apparent displacement of the centre of the rotation field can be due to distortions in a circular velocity field. Observations in the mid-IR (Acosta-Pulido et al. 2003) show that NGC 7582 presents both a nuclear bar and two nuclear spiral arms, which could be related to the observed distortions. The nuclear bar is oriented along PA ≈ 110–$290(-70)°$ extending from ≈ 1 arcsec E to ≈ 1 arcsec W from the nucleus, while the nuclear spiral arms are oriented approximately along the major axis of the galaxy and extending to ≈ 1.5 arcsec NW and SE of the nucleus. We show the orientation and extents of the nuclear bar and spiral as dotted and solid white lines, respectively, in Fig. 4. We note that the SE arm seems to correspond to the location where there seems to be an 'excess blueshift' in the stellar radial velocity field in Fig. 4.

The stellar velocity dispersion shows the highest values of ≈ 170 km s^{-1} to E and S of the nucleus (Fig. 4) which we interpret as representing the σ_* of the galaxy bulge. We use this value to estimate the mass of the SMBH (M_{BH}) of NGC 7582 from the relation $\log(M_{BH}/M_\odot) = \alpha + \beta \log(\sigma_*/\sigma_0)$, where $\alpha = 8.13 \pm 0.06$, $\beta = 4.02 \pm 0.32$ and $\sigma_0 = 200$ km s^{-1} (Tremaine et al. 2002). For $\sigma_* \approx 170$ km s^{-1}, we obtain $M_{BH} \approx 7 \times 10^7$ M$_\odot$, in good agreement with the value obtained by Wold et al. (2006b) through modelling of the kinematics of [Ne II] 12.8 μm emitting gas.

The σ_* map (Fig. 4) shows a region with low values ($\sigma_* \approx 50$ km s^{-1}) delineating a partial ring around the nucleus, which seems to be embedded in the bulge. These locations are close to those of the star clusters observed by Wold & Galliano (2006a), but somewhat displaced, being ≈ 50 pc closer to the nucleus. The lower σ_* values reveal that these stars have a 'colder kinematics' than that of the stars of the bulge. We note that these σ_* values are similar to those of the H$_2$ gas, suggesting that these stars have recently formed in the circumnuclear ring from kinematically cold gas, and which have not yet 'thermalized' with the 'hotter' stars in the bulge. But in order to present CO absorption, the stars should be at least 10^7 yr old (Oliva et al. 1995), what suggests that they belong to a previous burst of star formation and not the one which is presently ionizing the gas. This interpretation is supported by the displacement of this ring relative to that in the ionized gas, which suggests that the star formation is propagating outwards from the nucleus. Ring-like regions with low σ_* values have been observed also around other AGN (Barbosa et al. 2006; Riffel et al. 2008).

4.4 Gas kinematics

The radial velocity maps of both the Brγ and H$_2$ emitting gas (Fig. 5) are similar to the stellar one (Fig. 4). In order to better observe the possible differences, we have extracted one-dimensional cuts from the radial velocities maps which are shown in Fig. 10. These cuts were obtained by averaging the velocities within pseudo-slits of 0.45 arcsec width passing through the nucleus. The orientations of the slits were selected to provide a good coverage of the velocity fields, and are shown as dashed green lines in the bottom panel of Fig. 2. The top left-hand panel of Fig. 10 shows the velocities along PA $= -15(345) - 165°$, which is the orientation of the major

axis of the galaxy (Morris et al. 1985), while in the top right-hand panel we present the velocities along PA $= 23$–$203°$, in the bottom left-hand panel along PA $= 60$–$240°$ and in the bottom right-hand panel along PA $= 113$–$293°$.

The highest differences between the gaseous and stellar velocities are observed at 0.5–2.5 arcsec SW from the nucleus along PA $= 203°$, where the gaseous velocities reach values of up to -160 km s^{-1}, while the stellar velocities reach at most -100 km s^{-1}. For the PAs $165°$ and $240°$, the gaseous velocities are still more blueshifted than the stellar but only by about 40 km s^{-1} (to SE–SW of the nucleus). Along PA $= 293(-67)°$, to NW–W of the nucleus, the velocities observed for the stars are similar to those of the Brγ emitting gas, while the H$_2$ emitting gas is blueshifted by ≈ -20 km s^{-1}. We note that this orientation coincides with that of the nuclear bar, and suggest that, as this blueshift is observed against the far side of the Galactic plane, we could be observing an inflow of molecular gas towards the nucleus along the bar (which could be in the galaxy plane). We have already observed similar H$_2$ inflows towards the nucleus of another active galaxy, NGC 4051, not along a nuclear bar, but along a nuclear spiral arm (Riffel et al. 2008).

From Fig. 10, it can be concluded that the emitting gas is blueshifted relative to the stars to SW of the nucleus. This region is co-spatial with part of the [O III] ionization cone observed by Storchi-Bergmann & Bonatto (1991), shown by the green contours in Fig. 1. We interpret this excess blueshift as due to the contribution of gas outflowing from the nucleus to the total gas emission. We note that we are observing only a small fraction of the outflowing gas because the field of view of our observations is much smaller than the dimensions of the ionization cone, along which the gas is outflowing (Morris et al. 1985).

Figs 4, 5 and 10 suggest that the radial velocity field of the gas is similar to that of the stars except for the region along the ionization cone/nuclear outflow and possibly along the nuclear bar where there may be an H$_2$ inflow. In order to isolate the outflowing and inflowing components, we have subtracted the stellar velocity field from the Brγ and H$_2$ velocity fields. These residual maps are shown in Fig. 11. In the residual Brγ velocity map, the velocity values to NE–N–NW of the nucleus are close to zero, while to the S–SW–W the gas is blueshifted by up to -100 km s^{-1} relative to the stars. This velocity is of the order of those found by Morris et al. (1985) for the [O III] emitting gas. In the residual H$_2$ velocity map, the blueshift at PA $\approx 293(-67)$ can be observed in approximate alignment with the nuclear bar, whose orientation is shown as the white solid line in the bottom panel of Fig. 11.

Even higher blueshifts, of up to -350 km s^{-1}, are observed to the S–SW in the velocity channel maps (Fig. 6). The difference between the radial velocity maps and the velocity channel maps is due to the fact that the first gives the peak velocity of the emission line for a given spatial position, while the latter shows how the gas with a certain velocity is distributed along the narrow-line region (NLR). The peak wavelength will usually correspond to the kinematics of the component(s) with the highest flux(es), while the channel maps will also reveal weaker components which contribute to the wings of the emission-line profiles. We thus attribute the high blueshifts seen in the velocity channel maps to low-mass, high-velocity outflows, originated close to the nucleus which compress and push the gas further out to the observed radial velocities of ≈ -100 km s^{-1}. These high-velocity outflows do not appear in the radial velocity maps due to their low flux, appearing only as a blue wing to the profile, thus not affecting the peak wavelength used to derive the radial velocity. We have observed similar results in a recent study
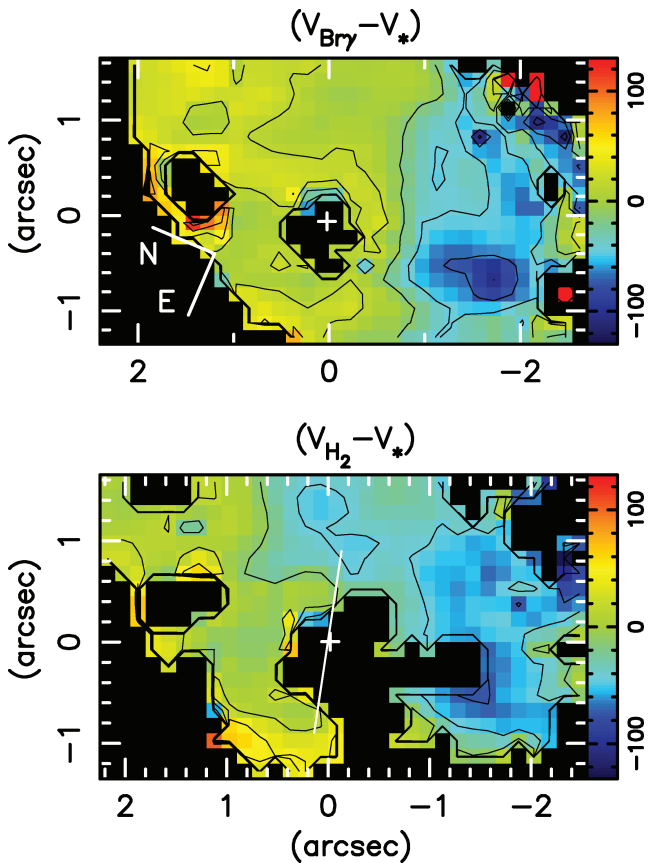
Figure 11. Residual maps obtained by the difference between the Brγ and H$_2$ radial velocity fields and the stellar one. The white line in the bottom panel shows the orientation and extent of the nuclear bar observed by Acosta-Pulido et al. (2003).

of the NLR of other nearby Seyfert galaxies using IFUs (Barbosa et al. 2009).

Outflows from the nucleus of active galaxies have been observed at optical wavelengths using long-slit spectroscopy (e.g. Storchi-Bergmann, Wiklson & Baldwin 1992; Crenshaw & Kraemer 2000; Das et al. 2005, 2006) and from radio observations (e.g. Morganti et al. 2007) and more recently by our group using IFUs (Riffel et al. 2006; Barbosa et al. 2009).

4.4.1 Mass outflow rates

We have used the velocity channel maps of Fig. 6 in order to estimate the mass outflow rate in the ionized gas. Inspecting these maps, it can be concluded that radial velocities of up to $\pm 200\,\mathrm{km\,s^{-1}}$ are observed to both sides of the nucleus, suggesting that up to these velocities, we are mapping gas motions in the galaxy disc. Above $200\,\mathrm{km\,s^{-1}}$, there are mostly blueshifts and almost no redshifts, what can be interpreted as due to the presence of outflows. Our interpretation for this result is that these outflows are seen in blueshift to the S–SW because they are partially oriented towards us and projected against the far side of the galaxy disc while the counterpart redshifted outflows are not seen because they are hidden behind the near side of the dusty disc. Thus, assuming that the emitting gas with blueshifts higher than $200\,\mathrm{km\,s^{-1}}$ is outflowing from the nucleus, we can estimate the mass outflow rate. In order to do this, we calculate the mass flux through a circular cross-section with a radius $r \approx 0.7$ arcsec at 1.2 arcsec from the nucleus, estimated from the

shape of the light distribution in the velocity channels corresponding to -308 and $-257\,\mathrm{km\,s^{-1}}$ in Fig. 6. The mass outflow rate has been calculated as $\dot{M}_\mathrm{H\,II} = 2m_\mathrm{p}N_\mathrm{e}v\pi r^2 f$, where m_p is the proton mass, N_e is the electron density, v is the velocity of the outflowing gas and f is the filling factor (Storchi-Bergmann et al. 2007; Riffel et al. 2008), and the factor of 2 is to take into account the likely presence of a hidden counterpart outflow to the one we observe. Adopting $N_\mathrm{e} = 100\,\mathrm{cm^{-3}}$ and $f = 0.001$ and adding the contribution of the two velocity bins above, we obtain $\dot{M}_\mathrm{H\,II} \approx 4.8 \times 10^{-2}\,\mathrm{M_\odot\,yr}$.

This outflow rate is somewhat smaller than those quoted in the literature for active galaxies, which are between 0.1 and $10\,\mathrm{M_\odot\,yr^{-1}}$ (e.g. Veilleux, Cecil & Bland-Hawthorn 2005). However, the latter values are generally obtained for objects with higher levels of activity than NGC 7582. For similar levels of activity and in comparable scales of hundreds of parsec, Barbosa et al. (2009) have obtained similar ionized gas outflow rates of $\approx 10^{-3}$ to $10^{-2}\,\mathrm{M_\odot\,yr^{-1}}$ from two-dimensional mapping of the gas kinematics in the central region of six nearby Seyfert galaxies, in good agreement with the value obtained here.

We now calculate the mass accretion rate necessary to produce the observed nuclear luminosity of NGC 7582. The latter can be estimated from $\dot{m} = \frac{L_\mathrm{bol}}{c^2 \eta}$, where L_bol is the bolometric luminosity, η is the efficiency of conversion of the rest mass energy of the accreted material into radiation and c is the speed of light. We adopt $\eta = 0.1$, a typical value for geometrically thin and optically thick accretion discs (e.g. Frank, King & Raine 2002) and use the relation $L_\mathrm{bol} \approx 20\,L_\mathrm{X}$ (Elvis et al. 1994), where $L_\mathrm{X} \approx 7.2 \times 10^{41}\,\mathrm{erg\,s^{-1}}$ is the hard X-ray luminosity (Piconcelli et al. 2007). The result is $\dot{m} \approx 2.6 \times 10^{-3}\,\mathrm{M_\odot\,yr^{-1}}$.

Comparing the mass outflow rate with the accretion rate calculated above, it can be concluded that the former is an order of magnitude larger than the latter, a relation similar to those reported by Veilleux et al. (2005) for more luminous active galaxies, as well as to those obtained by Barbosa et al. (2009) for other nearby Seyfert galaxies and to that obtained by Crenshaw & Kraemer (2007) for the Seyfert galaxy NGC 4151.

4.4.2 Feeding versus feedback

Although there are similarities between the velocity fields observed for H$_2$ and Brγ, there are also differences in the detailed kinematics for the two gas phases, as follows. (i) The small but systematic excess blueshift in the H$_2$ emitting gas along PA $= 293(-67)°$, suggests that there could be an inflow of molecular gas along a nuclear bar, as discussed above. (ii) The Brγ σ map (Fig. 5) shows the highest values to the S–SE of the nucleus, approximately at the same location where the highest blueshifts are observed (see Fig. 11). This result supports an origin for at least part of the Brγ emission of this region in disturbed gas which is not confined to the galaxy plane but is outflowing from the nucleus along the ionization cone seen in [O III]. The H$_2$ σ map, on the other hand, presents overall lower σ values consistent with a dominant origin in molecular gas orbiting in the plane of the galaxy. (iii) The velocity channel maps shown in Figs 6 and 7 also support a larger contribution from outflowing gas to the Brγ than to the H$_2$ emission, since the blueshifted emission in Brγ reaches larger velocity values and is found farther away from the line of nodes than in the H$_2$ emitting gas.

Previous studies have also found that the H$_2$ traces less disturbed kinematics than the ionized gas in the circumnuclear region of Seyfert galaxies (Storchi-Bergmann et al. 1999; Rodríguez-Ardila et al. 2004, 2005a; Riffel et al. 2006, 2008), leading to the suggestion that the molecular gas, orbiting in the plane, traces the feeding of

the active nucleus via the inflow of cold gas, while the ionized gas traces its feedback via the outflows. In Riffel et al. (2008), we could trace streaming motions in the H_2 emitting gas towards the nucleus along a nuclear spiral arm. In the present observations, there is also some evidence of inflow along a nuclear bar. The compactness and high inclination of the circumnuclear ring of star formation does not favour the detection of possible additional streaming motions between the ring and the nucleus. The H_2 flux distribution shows that the molecular gas is not concentrated in the star-forming ring, but is distributed over the whole nuclear region, indicating the presence of similar density of molecular gas at the ring and between the nucleus and the ring. This molecular gas could be the material which is feeding and probably will continue to feed the active nucleus for some time in the future.

4.4.3 AGN–starburst connection in NGC 7582

The total mass of the hot H_2 in the nuclear region of NGC 7582 can be estimated as (Riffel et al. 2008)

$$\left(\frac{M_{H_2}}{M_\odot}\right) = 2.40 \times 10^{14} \left(\frac{F_{H_2\lambda2.2235}}{erg\ s^{-1}\ cm^{-2}}\right) \left(\frac{d}{Mpc}\right)^2, \qquad (8)$$

where we assume a vibrational temperature of $T_{vib} = 2000\,K$, which implies a population fraction $f_{v=1,J=2} = 3.7 \times 10^{-3}$ (Scoville et al. 1982) and a transition probability $A_{S(0)} = 2.53 \times 10^{-7}\ s^{-1}$ (Turner, Kirby-Docken & Dalgarno 1977). Integrating the flux of the $H_2\lambda2.2235\,\mu m$ emission line over the whole IFU field, we obtain $F_{H_2\lambda2.2235} \approx 5.5 \times 10^{-15}\ erg\ s^{-1}\,cm^{-2}$ and thus $M_{H_2} \approx 620\,M_\odot$.

The above value is the mass of the hot H_2 emitting gas, which is probably only the 'hot skin' of the molecular gas available in the nuclear region to feed the active nucleus. The total mass of molecular gas should be much higher, as it should be dominated by cold gas, which has been estimated to be 10^5 to 10^7 times that of the hot gas in galaxies for which both hot and cold molecular gas have been observed (Dale et al. 2005). Thus, there should be plenty of molecular gas, not only to feed the AGN but also to give origin to the recent bursts of star formation in the ring.

The molecular gas accumulated in the nuclear region was probably the fuel which gave origin to the nuclear ring of star formation, as well as to the present episode of nuclear activity. Although both the star formation and nuclear activity could have been triggered simultaneously, there is also the possibility that the star formation was triggered first, and then the mass loss from stellar winds and supernova explosions in the CNSFRs have been the source of fuel for the SMBH. It is thus instructive to estimate the available mass to feed the SMBH under the above assumption. For solar metallicity and an age of 5 Myr, the total mass loss for the two CNSFRs is in the range $\approx 10^3$–$10^5\,M_\odot$ (Leitherer & Heckman 1995). Assuming a value of $10^4\,M_\odot$, and that the duration of this process is a few 10^6 yr, one gets a rate of mass loss of $10^{-2}\,M_\odot\ yr^{-1}$. (Note that this value is ≈ 5 times larger than the nuclear accretion rate calculated above, of $\dot{m} \approx 2.6 \times 10^{-3}\,M_\odot\ yr^{-1}$, within the uncertainties of the calculations.) If this mass reaches the nucleus along a nuclear bar (as observed in NGC 7582) or nuclear spiral arms [as observed in NGC 1097 (Fathi et al. 2006) and NGC 6951 (Storchi-Bergmann et al. 2007)], with velocities of ≈ 20–$60\ km\ s^{-1}$, then this gas would take a few 10^6 yr to reach the nucleus. This time-scale allows for the coexistence of the nuclear activity and the star-forming regions of 5 Myr under the hypothesis that the nuclear activity has been triggered by mass accretion originated from mass loss of young stars formed in the circumnuclear ring. Alternatively, the triggering may have happened during a previous burst of star formation in the

ring. The presence of such previous starburst is supported by the partial ring of low σ_* observed in the stellar kinematics. In addition, as pointed out in Section 4.1, the extranuclear spectrum does not differ significantly from those of the star-forming ring, suggesting that there may be regions of recent star formation even closer to the nucleus, which may be contributing to the SMBH feeding as well.

Finally, we quantify the AGN–starburst connection in NGC 7582 by comparing the mass accretion rate to the SMBH with the SFR in the circumnuclear region. As pointed out in Introduction, the M–σ relation implies that the mass of the SMBH in galaxies grows in proportion to the growth of the bulge. If the bulge grows via star formation episodes, the mass accretion rate to the SMBH should be proportional to the SFR. Which should be the ratio between the mass accretion rate and the SFR? The same as between the mass of the SMBH and the mass of the host galaxy bulge, which was first obtained by Magorrian et al. (1998), and today known as the Magorrian relation (Ferrarese & Merrit 2001), which has been revised to a ratio of 0.1 per cent between the mass of the SMBH and that of the bulge. Assuming that the total SFR can be represented by that of the ring, we get for NGC 7582 a ratio of 0.26 per cent between the mass accretion rate and the SFR, a number which is close to that of the Magorrian relation, considering the uncertainties. These uncertainties include, in particular, a possible underestimate of the SFR in the nuclear region, as our observation misses the top border of the star-forming ring, and a possible contribution of a starburst included within the nuclear aperture.

5 SUMMARY AND CONCLUSIONS

Two-dimensional near-IR K-band spectroscopy from the inner $660 \times 315\ pc^2$ of the Seyfert galaxy NGC 7582, obtained with the Gemini GNIRS IFU at a spatial resolution of $\approx 40\ pc^2$ and spectral resolution of $\approx 3\,\text{Å}$, was used to map the molecular and ionized gas emission-line flux distributions and kinematics as well as the stellar kinematics. The region covered by the observations includes most of a circumnuclear ring of star formation in the plane of the galaxy plus a small part of an outflow extending to high galactic latitudes.

Our main conclusions are as followed.

(i) The nucleus contains an unresolved source whose continuum is well reproduced by a blackbody function with temperature $T \approx 1050\,K$, which we attribute to emission by the circumnuclear dust heated by the AGN, with an estimated mass of $\approx 3 \times 10^{-3}\,M_\odot$ located within 25 pc of the nucleus. The nuclear spectrum also shows a broad component in the $Br\gamma$ emission line with FWHM $\approx 3900\ km\ s^{-1}$.

(ii) The $Br\gamma$ flux distribution is dominated by emission from a circumnuclear ring of star formation, previously seen only in mid-IR observations, with a radius of $\approx 190\ pc$, which contributes with ≈ 80–90 per cent of the $Br\gamma$ emission, the rest being contributed by the nuclear source. Two large star-forming regions with an age ≈ 5 Myr contribute with 50 per cent of the $Br\gamma$ emission of the ring, resulting in ≈ 1000 O6 stars per region and a star-forming rate of $\approx 0.25\,M_\odot\ yr^{-1}$. The total rate of ionizing photons emitted by the ring is $\approx 10^{53}\ s^{-1}$, the total star-forming rate is $\approx 1\,M_\odot\ yr^{-1}$ and the total mass of ionized gas is $\approx 3 \times 10^6\,M_\odot$.

(iii) The H_2 flux distribution is more uniformly distributed over the nuclear region than the $Br\gamma$ flux distribution and gives a mass of hot molecular gas of $\approx 620\,M_\odot$. From previous studies, it can be concluded that the total mass of H_2 gas (which is dominated by the cold H_2) can be 10^5–10^7 times larger.

(iv) The stellar velocity field shows a distorted rotation pattern whose centre appears to be displaced up to 50 pc from the nucleus (identified as the peak of the continuum emission). The distortion could be associated to a nuclear bar and a nuclear spiral previously seen in mid-IR images. The velocity dispersion of the bulge is $\sigma_* \approx 170\,\mathrm{km\,s^{-1}}$, implying in a mass of $M_{BH} \approx 7 \times 10^7\,M_\odot$ for the SMBH, in good agreement with previous determinations. Immersed in this bulge, there is a partial ring of lower $\sigma_* (\approx 50\,\mathrm{km\,s^{-1}})$, which is close to the star-forming ring but displaced ≈ 50 pc inwards. As the velocity dispersion is similar to that of the molecular gas, this ring can be interpreted as due to stars recently formed from cold gas, although in a previous burst (age $\geq 10^7$ yr), still keeping the gas kinematics as they did not have time yet to 'thermalize' with the stars of the bulge.

(v) The radial velocity field of the ionized gas is similar to that of the stellar component to the N–NW, while to the S–SW there is an additional blueshifted component ($v \approx -100\,\mathrm{km\,s^{-1}}$), which we attribute to outflows along the ionization cone (previously observed in a narrow-band [O III] image) which is partially covered by our observations. Velocity channel maps along the Brγ emission-line profile show even higher blueshifts, reaching $v \approx -300\,\mathrm{km\,s^{-1}}$ in the outflow, while the maximum redshift observed is $v \approx 200\,\mathrm{km\,s^{-1}}$. The velocity dispersion is enhanced in the region of the outflow.

(vi) The mass outflow rate in the ionized gas is estimated to be $\dot{M}_{HII} \approx 0.05\,M_\odot\,\mathrm{yr^{-1}}$, which is an order of magnitude larger than the accretion rate to feed the AGN, a ratio which is similar to those found in other AGN. This large ratio indicates that the outflowing gas does not originate in the AGN, but is instead the circumnuclear gas from the host galaxy being pushed away by a nuclear outflow.

(vii) The kinematics of the hot molecular gas, traced by the H$_2$ emission, shows smaller blueshifts along the outflow as well as lower velocity dispersions, which suggests most of the molecular gas is in the Galactic plane. An excess blueshift along PA $\approx -70°$, where a nuclear bar has been observed, can be interpreted as an inflow towards the nucleus. We thus conclude that the H$_2$ kinematics traces the feeding of the AGN, while the ionized gas kinematics traces its feedback via the outflows.

(viii) The estimated mass-loss rate from the evolving stars in the circumnuclear ring is $\approx 10^{-2}\,M_\odot\,\mathrm{yr^{-1}}$, which is ≈ 5 times the nuclear accretion rate. As the estimated time for this mass to reach the nucleus is a few 10^6 yr, this material could be the fuel which just triggered the nuclear activity. Nevertheless, as there is also a previous burst of star formation almost co-spatial with the ring, the fuel may have been available previously (e.g. $\approx 10^7$ yr). In addition, previous data suggest that there may also be recent star formation inside the ring, closer to the nucleus.

(ix) We conclude that the AGN–starburst connection in NGC 7582 may have occurred in two ways: (i) there is a large molecular gas reservoir in the nuclear region which gave origin to both the star formation in the circumnuclear ring and the nuclear activity and (ii) the molecular gas has given origin first to circumnuclear star formation and the mass loss from the evolving stars has then triggered the nuclear activity.

(x) The ratio between the mass accretion rate and the SFR in the circumnuclear region, of 0.26 per cent, is close to the value implied by the Magorrian relation between the mass of the SMBH and the mass of the bulges of the host galaxies. This result shows that a growth of the SMBH proportional to the growth of the bulge can proceed via circumnuclear star formation around AGN.

REFERENCES

Acosta-Pulido J. A., Pérez García A. M., Prieto M. A., Rodríguez-Espinosa J. M., Cairós L. M., 2003, RMxAC, 16, 198

Allington-Smith J. R., Content R., Dubbeldam C. M., Robertson D. J., Preuss W., 2006, MNRAS, 371, 380

Allington-Smith J. et al., 2007, MNRAS, 376, 785

Aretxaga I., Joguet B., Kunth D., Melnick J., Terlevich R. J., 1999, ApJ, 519, L123

Barbosa F. K. B., Storchi-Bergmann T., Cid Fernandes R., Winge C., Schmitt H., 2006, MNRAS, 371, 170

Barbosa F. K. B., Storchi-Bergmann T., Cid Fernandes R., Winge C., Schmitt H., 2009, MNRAS, in press

Baribaud T., Alloin D., Glass I., Pelat D., 1992, A&A, 256, 375

Barvainis R., 1987, ApJ, 320, 537

Cappellari M., Emsellem E., 2004, PASP, 116, 138

Cardelli J. A., Clayton G. C., Mathis J. S., 1989, ApJ, 345, 245

Cid Fernandes R., Terlevich R., 1995, MNRAS, 272, 423

Cid Fernandes R., Heckman T., Schmitt H., González Delgado R. M., Storchi-Bergmann T., 2001, MNRAS, 558, 81

Cid Fernandes R., González Delgado R. M., Storchi-Bergmann T., Martins L. Pires, Schmitt H., 2005, MNRAS, 356, 270

Clavel J., Wamsteker W., Glass I. S., 1989, ApJ, 337, 236

Crenshaw D. M., Kraemer S. B., 2000, ApJ, 532, L101

Crenshaw D. M., Kraemer S. B., 2007, ApJ, 659, 250

Dale D. A., Sheth K., Helou G., Regan M. W., Hüttemeister S., 2005, ApJ, 129, 2197

Das V. et al., 2005, AJ, 130, 945

Das V., Crenshaw D. M., Kraemer S. B., Deo R. P., 2006, AJ, 132, 620

Davies R. I., Sternberg A., Lehnert M. D., Tacconi-Garman L. E., 2005, ApJ, 633, 105

Davies R. I., Mueller Sánchez F., Genzel R., Tacconi L. J., Hicks E. K. S., Friedrich S., Sternberg A., 2007, ApJ, 671, 1388

de Vaucouleurs G., de Vaucouleurs A., Corwin H. G., Jr, Buta R. J., Paturel G., Fouque P., 1991, Sky Telesc., 82, 621

Dors O. L., Jr., Storchi-Bergmann T., Riffel R. A., Schimdt A. A., 2008, A&A, 482, 59

Elias J. H. et al., 1998, in Fowler A. M., ed., Infrared astronomical instrumentation. Proc. SPIE, 3354, 555

Emsellem E. et al., 2004, MNRAS, 352, 721

Elvis M. et al., 1994, ApJS, 95, 1

Fathi K., Storchi-Bergmann T., Riffel R. A., Winge C., Axon D. J., Robinson A., Capetti A., Marconi A., 2006, ApJ, 641, L25

Ferrarese L., Merrit D., 2000, ApJ, 539, L9

Ferrarese L., Merrit D., 2001, MNRAS, 320, L30

Frank J., King A. R., Raine D. J., 2002, Accretion Power in Astrophysics, 3rd edn. Cambridge Univ. Press, Cambridge

Galliano E., Alloin D., 2008, A&A, 487, 519

Ganda K., Falcón-Barroso J., Peletier R. F., Cappellari M., Emsellem E., McDermid R. M., de Zeeuw P. T., Carollo C. M., 2006, MNRAS, 367, 46

Gebhardt K. et al., 2000, ApJ, 543, L5

Gerssen J., Allington-Smith J., Miller B. W., Turner J. e. H., Walker A., 2006, MNRAS, 365, 29

Glass I., 1992, MNRAS, 256, 23P

González Delgado R. M., Heckman T., Leitherer C., Meurer G., Krolik J., Wilson A. S., Kinney A., Koratkar A., 1998, ApJ, 505, 174

Granato G. L., Danese L., 1994, MNRAS, 268, 235

Hägele G. F., Díaz A. I., Cardaci M. V., Terlevich E., Terlevich R., 2007, MNRAS, 378, 163

Hameed S., Devereux N., 1999, AJ, 118, 730

Heckman T. M., González-Delgado R., Leitherer C., Meurer G. R., Krolik J., Wilson A. S., Koratkar A., Kinney A., 1997, ApJ, 482, 114

Jaffe W. et al., 2004, Nat, 429, 47

Kauffmann G. et al., 2003, MNRAS, 346, 1055

Kennicutt R. C., 1998, ARA&A, 36, 189

Leitherer C., Heckman T. M., 1995, ApJS, 96, 9

Magorrian J. et al., 1998, AJ, 115, 2285

Marco O., Alloin D., 1998, A&A, 336, 823

Marco O., Alloin D., 2000, A&A, 353, 465

Morris S., Ward M., Whittle M., Wilson A. S., Taylor K., 1985, MNRAS, 216, 193

Morganti R., Holt J., Saripalli L., Oosterloo T. A., Tadhunter C. N., 2007, A&A, 476, 735

Norman C., Scoville N., 1988, ApJ, 332, 124

Oliva E., Origlia L., Kotilainen J. K., Moorwood A. F. M., 1995, A&A, 301, 55

Osterbrock D. E., 1989, Astrophysics of Gaseous Nebulae and Active Galactic Nuclei. University Science Books, Mill Valley, California

Piconcelli E., Bianchi S., Guainazzi M., Fiore F., Chiaberge M., 2007, A&A, 466, 855

Regan M. W., Mulchaey J. S., 1999, AJ, 117, 2676

Perry J. J., Dyson J. E., 1985, MNRAS, 213, 665

Riffel R. A., Sorchi-Bergmann T., Winge C., Barbosa F. K. B., 2006, MNRAS, 373, 2

Riffel R. A., Storchi-Bergmann T., Winge C., McGregor P. J., Beck T., Schmitt H., 2008, MNRAS, 385, 1129

Rodríguez-Ardila A., Mazzalay X., 2006, MNRAS, 367, L57

Rodríguez-Ardila A., Pastoriza M. G., Viegas S., Sigut T. A. A., Pradhan A. K., 2004, A&A, 425, 457

Rodríguez-Ardila A., Riffel R., Pastoriza M. G., 2005a, MNRAS, 364, 1041

Rodríguez-Ardila A., Contini M., Viegas S., 2005b, MNRAS, 357, 220

Santos-Lléo M., Clavel J., Barr P., Glass I. S., Pelat D., Peterson B. M., Reichert G., 1995, MNRAS, 274, 1

Schmitt H. R., Kinney A. L., 2000, ApJS, 128, 479

Schmitt H. R., Storchi-Bergmann T., Cid Fernandes R., 1999, MNRAS, 303, 173

Scoville N. Z., Hall D. N. B., Kleinmann S. G., Ridgway S. T., 1982, ApJ, 253, 136

Simões Lopes R. D., Storchi-Bergmann T., de Fátima Saraiva M., Martini P., 2007, ApJ, 655, 718

Shi L., Gu Q. S., Peng Z. X., 2006, A&A, 450, 15

Sosa-Brito R. M., Tacconi-Garman L. E., Lehnerth M. D., Galimore J. F., 2001, ApJS, 136, 61

Storchi-Bergmann T., Bonatto C. J., 1991, MNRAS, 250, 138

Storchi-Bergmann T., Wiklson A. S., Baldwin J. A., 1992, ApJ, 396, 45

Storchi-Bergmann T., Winge C., Ward, m. J., Wilson A. S., 1999, MNRAS, 304, 35

Storchi-Bergmann T., González Delgado R. M., Schmitt H. R., Cid Fernandes R., Heckman T., 2001, ApJ, 559, 147

Storchi-Bergmann T., Nemmen R. S., Spinelli P. F., Eracleous M., Wilson A. S., Filippenko A. V., Livio M., 2005, ApJ, 624, 13

Storchi-Bergmann T., Dors O. L., Riffel R. A., Fathi K., Axon D. J., Robinson A., Marconi A., Östlin G., 2007, ApJ, 670, 959

Terlevich R., Melnick J., 1985, MNRAS, 213, 841

Tremaine S. et al., 2002, ApJ, 574, 740

Turner J., Kirby-Docken K., Dalgarno A., 1977, ApJS, 35, 281

Veilleux S., Cecil G., Bland-Hawthorn J., 2005, ARA&A, 43, 769

Winge C., Riffel R. A., Storchi-Bergmann T., 2007, preprint (http://www.gemini.edu/sciops/instruments/nir/spectemp/index.html)

Wold M., Galliano E., 2006, MNRAS, 369, 47

Wold M., Lacy M., Käufl H. U., Siebenmorgen R., 2006, A&A, 460, 449

This paper has been typeset from a TEX/LATEX file prepared by the author.